J. Fluid Mech. (1987), *vol.* 178, *pp.* 195–219
Printed in Great Britain

Numerical simulations of nonlinear axisymmetric flows with a free surface

By DOUGLAS G. DOMMERMUTH AND DICK K. P. YUE
Department of Ocean Engineering, Massachusetts Institute of Technology, Cambridge, MA 02139, USA

(Received 25 June 1986)

A numerical method is developed for nonlinear three-dimensional but axisymmetric free-surface problems using a mixed Eulerian–Lagrangian scheme under the assumption of potential flow. Taking advantage of axisymmetry, Rankine ring sources are used in a Green's theorem boundary-integral formulation to solve the field equation; and the free surface is then updated in time following Lagrangian points. A special treatment of the free surface and body intersection points is generalized to this case which avoids the difficulties associated with the singularity there. To allow for long-time simulations, the nonlinear computational domain is matched to a transient linear wavefield outside. When the matching boundary is placed at a suitable distance (depending on wave amplitude), numerical simulations can, in principle, be continued indefinitely in time. Based on a simple stability argument, a regriding algorithm similar to that of Fink & Soh (1974) for vortex sheets is generalized to free-surface flows, which removes the instabilities experienced by earlier investigators and eliminates the need for artificial smoothing. The resulting scheme is very robust and stable.

For illustration, three computational examples are presented: (i) the growth and collapse of a vapour cavity near the free surface; (ii) the heaving of a floating vertical cylinder starting from rest; and (iii) the heaving of an inverted vertical cone. For the cavity problem, there is excellent agreement with available experiments. For the wave–body interaction calculations, we are able to obtain and analyse steady-state (limit-cycle) results for the force and flow field in the vicinity of the body.

1. Introduction

Ever since the work of Longuet-Higgins & Cokelet (1976), the mixed Eulerian–Lagrangian method has been used efficaciously for a variety of nonlinear free-surface problems in two dimensions. The algorithm requires two steps: at any instant of time, the field equation is solved in an Eulerian frame, after which Lagrangian points are followed on the free surface to update their positions and potential values. The first step is typically accomplished by writing a boundary-integral equation for the velocity potential, and the second by high-order finite-difference time integrators.

Assuming periodic waves, Longuet-Higgins & Cokelet (1976) were able to simulate propagating steep Stokes' waves, as well as realistic overturning and plunging of the wave crest when an asymmetric surface pressure was applied. Faltinsen (1977) applied a similar method to study the nonlinear waves outside and inside moving bodies. For the former, periodic boundary conditions were replaced in favour of matching to a Rankine (non-wave) potential in the far field. Vinje & Brevig (1981) extended the approach of Longuet-Higgins & Cokelet to include finite water depth

and floating bodies but retained the assumption of spatial periodicity. By applying Cauchy's integral theorem to the complex potential they were able to obtain Fredholm integral equations of the second kind for both the stream function on the free surface and the potential on the body, resulting in a substantial gain in efficiency and accuracy of the equation system. The same idea was exploited by Baker, Meiron & Orszag (1982) who used a dipole distribution on the free-surface (where Dirichlet conditions are posed), and the resulting Fredholm equations of the second kind were solved using an iterative method. Unlike the complex-potential formulation of Vinje & Brevig, this approach can, in principle, be extended directly to three-dimensional problems.

In this paper, we extend the semi-Lagrangian method to vertically axisymmetric free-surface flows. Our ultimate (but ambitious) objective is to be able to simulate fully three-dimensional nonlinear interactions between a free-surface and a body. A number of important difficulties remain to be resolved before such a goal can realistically be reached (see §5). In the present context of axisymmetric problems, we are able to address and satisfactorily solve three of the main outstanding problems: (i) implementation of a far-field closure; (ii) treatment of the body and free-surface intersection line; and (iii) stable representation and time integration of the free surface. In addition, through a number of computational examples, the usefulness and accuracy of the mixed Eulerian–Lagrangian approach to problems in more than two dimensions is demonstrated. This research paves the way for numerical study of nonlinear three-dimensional diffraction and radiation problems of scientific and engineering importance.

1.1. *Far-field closure*

A satisfactory treatment of the far-field condition is essential to the study of exterior-wave-motion problems. When the physical problem possesses spatial periodicity, such a difficulty is easily resolved by using periodic boundary conditions (e.g. Longuet-Higgins & Cokelet 1976). The computation domain is folded onto itself and the exterior (periodic) boundaries are simply eliminated. When an isolated body is present in an unbounded region, the assumptions of spatial periodicity or of fixed boundaries at some distance are clearly unrealistic. Nevertheless, by keeping a relatively large domain, Vinje & Brevig (1981), Greenhow *et al.* (1982) and others were able to use periodic conditions to study the dynamics of a floating body.

Faltinsen (1977) in his study of the heaving motion of a two-dimensional floating body, matched his nonlinear inner solution to that of a Rankine dipole in the far field. Since wave effects are not present in the latter, Faltinsen found that unless the interior computational domain was increased as a function of simulation time, the computations would soon break down. Assuming a boundary-integral formulation for the nonlinear interior domain with N free-surface points, N must increase approximately linearly with time T for both of the above approaches with the associated $O(N^2)$ and $O(N^3)$ increases in storage and computational effort per time-step (assuming a direct solution) respectively. For this reason, the cost may become prohibitive even for two-dimensional problems, and Faltinsen's results, for example, were typically restricted to less than one oscillation period. The situation is even more critical for three-dimensional problems with the anticipated $O(T^2, T^4, T^6)$ increase respectively in unknowns N, storage, and number of operations per time-step. Thus, in Isaacson's (1982) Eulerian calculation of the nonlinear diffraction by a vertical cylinder, where the fluid velocities were assumed to be zero on a finite truncation boundary, motion for only a fraction of a wave period could be simulated.

In this work, we pose a far-field closure by matching the nonlinear computational solution to a general linear solution of transient outgoing radiated waves. The determination of the linear wavefield as well as specification of the boundary condition for the nonlinear interior problem are obtained through a matching of the two on a fictitious boundary some distance away. Such a scheme is, in principle, untenable in two-dimensional flows since the nonlinearity of the radiated waves persists into the far field, and a simple matching to linear outer solutions is problematic (e.g. Vinje, Maogang & Brevig 1982). In three dimensions, however, the energy density of the radiating waves must necessarily decrease with radial distance so that a matching to a general linear solution is in theory valid at least some distance away. Indeed, for a suitably fixed matching radius (based for example only on motion amplitude) nonlinear simulations can in principle be carried out indefinitely in time. This is confirmed by our numerical experiments where we are able to continue the computations until steady-state conditions are reached for the entire inner computation domain (see §4).

1.2. *Body and free-surface intersection line*

A confluence of boundary conditions exists at the intersection of the free surface and a body moving in it. As a result, the solution exhibits a weak singularity at that point. According to linear theory, the velocity potential for a vertical wall moving horizontally is logarithmically singular at the contact point (Kravtchenko 1954), and a similar singularity is also present for general three-dimensional flows (Miloh 1980). This singularity persists even when full nonlinearity is introduced. For example, for a vertical two-dimensional piston moving in a water depth h, D. H. Peregrine (1972, unpublished notes) derived a perturbation result where the surface elevation displayed a $t \log(\tanh(\pi x/4h))$ behaviour for small time t, where x is the horizontal coordinate measured from the wavemaker. This two-dimensional result has been confirmed by a number of other investigations using both Eulerian and Lagrangian analyses as well as by experiments, and are reviewed in Greenhow & Lin (1983) and Lin (1984). Computationally, this weak singularity along the intersection line has a global influence and numerical difficulties for the nonlinear problem can be expected there. In Vinje & Brevig (1981), the intersection point was treated as part of the body boundary where a kinematic condition but not the free-surface conditions were prescribed, and the position and potential at that point were subsequently obtained via extrapolation. The results using this approach were not completely satisfactory, and in a later work by Greenhow *et al.* (1982) using the same method, they found it necessary to use experimental measurements to fix the intersection-point locations in their computations to produce acceptable results.

For two-dimensional problems, Lin (1984) developed a novel approach where, by specifying both the stream function and the velocity potential at the intersection point in the Cauchy integral-equation solution, the computational difficulties there were, in practice, avoided. In this paper, we adopt a similar idea for the axisymmetric problem where the field equation is solved in terms of the velocity potential and its normal derivative. The resulting scheme is robust and effective as demonstrated, for example, by our computations of a heaving inverted cone (see §4).

1.3. *Stability of the free surface*

In the original work of Longuet-Higgins & Cokelet (1976), a 'sawtooth' instability of the free surface was encountered and a smoothing technique was employed to suppress its development. Since then similar smoothing methods have been found

necessary by many investigators especially when the local steepness of the waves is large. It is now believed that such high-wavenumber instabilities are non-physical and are closely related to the accuracy of the velocity calculations for the free-surface particles. The exact mechanism of the instability is, however, quite subtle and may well depend on the details of a particular implementation. In Vinje & Brevig (1981)'s computations using Cauchy's integral formula, no such instability was observed, although using essentially similar schemes Baker *et al.* (1982) and Lin, Newman & Yue (1984) both required a smoothing operator to suppress instabilities when the waves were steep. On the other hand, when a dipole (rather than vortex) distribution was used in Baker *et al.* the instability was found to be greatly reduced. Roberts (1983) analysed this problem using Fourier spectral representations for the position and potential of a free-shear layer and was able to remove the numerical instability by a simple modification of the highest (even) Fourier mode. Dold & Peregrine (1986) extended the idea of Vinje & Brevig (1981) by calculating also the higher time derivatives of the complex potential in the Eulerian step. The resulting time integration scheme had an improved accuracy but more importantly showed only minor short-wavelength instabilities which were easily controlled, without resorting to smoothing, by decreasing the time-step size. Such a scheme is somewhat analogous to a modified Runge–Kutta integration where new values of the potential but not the free-surface positions are used in the intermediate steps of the integration (see §3).

We postulate (see §3) that a root cause of the high-wavenumber instability is the concentration of Lagrangian markers in the region of higher gradients, so that for a fixed time-step a local Courant condition is inevitably violated as the wave steepens (as evident, for example, in the numerical experiments of Dold & Peregrine 1986, §6). Thus, we develop a regriding algorithm wherein a new set of equally spaced (in arclength) Lagrangian points on the free surface are created after every time-step. Such an idea is not new and is not unlike, for example, that used by Fink & Soh (1974) in their simulation of thin vortex sheets. Our numerical experiments indicate that the regriding method is extremely effective and eliminates the instabilities without the use of *artificial* smoothing. Although regriding effectively acts as a nonlinear smoothing process to suppress instabilities (Moore 1981), as explained in §3 a regriding approach has important advantages over the traditional smoothing techniques especially in conjunction with a careful treatment of the free surface and body intersection line.

2. Mathematical formulation

We consider the irrotational flow of an incompressible, inviscid fluid with a free surface. The flow can be described by a velocity potential $\phi(\boldsymbol{x}, t)$ and the fluid velocity is given by $\boldsymbol{v} = \nabla\phi$. Inside the fluid volume $V(t)$, ϕ satisfies Laplace's equation

$$\nabla^2\phi = 0 \quad \text{in } V(t). \tag{2.1}$$

On the free surface $F(\boldsymbol{x}, t)$, ϕ satisfies the kinematic boundary condition

$$\frac{\mathrm{D}\boldsymbol{x}}{\mathrm{D}t} \equiv \left(\frac{\partial}{\partial t} + \boldsymbol{v}\cdot\nabla\right)\boldsymbol{x} = \nabla\phi \quad \text{on } F(\boldsymbol{x}, t) \tag{2.2a}$$

and the dynamic boundary condition (assuming zero atmospheric pressure)

$$\frac{\mathrm{D}\phi}{\mathrm{D}t} = -gz + \tfrac{1}{2}|\nabla\phi|^2 \quad \text{on } F(\boldsymbol{x}, t), \tag{2.2b}$$

where g is the acceleration due to gravity, the vertical coordinate z is positive up, and $z = 0$ is the undisturbed water surface. On the body surface $B(\boldsymbol{x}, t)$, the normal velocity is continuous,

$$\nabla\phi \cdot \boldsymbol{n}(\boldsymbol{x}, t) \equiv \frac{\partial\phi}{\partial n} = U(\boldsymbol{x}, t) \text{ prescribed}, \quad \text{on } B(\boldsymbol{x}, t), \tag{2.3}$$

where $\boldsymbol{n}$ is the unit normal pointing out of the fluid and n the coordinate along $\boldsymbol{n}$. On a stationary horizontal bottom B_0 at $z = -h$, (2.3) is satisfied there with $U = 0$. In addition, we specify zero initial conditions and a suitable far-field condition

$$\phi \to 0 \quad \text{as } |\boldsymbol{x}| \to \infty, \quad t < \infty. \tag{2.4}$$

We further establish a vertical circular cylindrical matching surface S_0, of a fixed radius A, enclosing B. From (2.1), we have from Green's identity

$$\alpha(\boldsymbol{x}, t)\,\phi(\boldsymbol{x}, t) = \iint_{S(t)} \left(\frac{\partial\phi}{\partial n'} - \phi\frac{\partial}{\partial n'}\right)\frac{1}{R}\,\mathrm{d}\boldsymbol{x}', \quad \boldsymbol{x} \in S, \tag{2.5}$$

where $R = |\boldsymbol{x} - \boldsymbol{x}'|$, $S(t) = B \cup \overline{B}_0 \cup \overline{F} \cup S_0$, the overbar denotes that portion of the surface enclosed by S_0, α is the included solid angle at $\boldsymbol{x}$, and the exclusion of the singular point $\boldsymbol{x}$ from the integral is always implied.

For axisymmetric bodies and motion, and assuming that the radiated waves are circumferentially stable, it follows from (2.3) that ϕ and F are also independent of the angular coordinate θ and (2.5) can be integrated in θ to give

$$\alpha(r, z, t)\,\phi(r, z, t) = \int_{\partial S} r'\left(\frac{\partial\phi}{\partial n'} - \phi\frac{\partial}{\partial n'}\right)G(r, z; r', z')\,\mathrm{d}\boldsymbol{x}', \quad (r, z) \in \partial S. \tag{2.6}$$

The line integral is along the trace $\partial S(t) = \partial B \cup \partial\overline{B}_0 \cup \partial\overline{F} \cup \partial S_0$ of S on (r, z). G is the Rankine ring source given by

$$G(r, z, ; r', z') = \int_0^{2\pi} \frac{\mathrm{d}\theta'}{R} = \frac{4}{\rho_1} K\left(1 - \frac{\rho^2}{\rho_1^2}\right), \tag{2.7}$$

where $\rho^2 = (z - z')^2 + (r - r')^2$, and $\rho_1^2 = (z - z')^2 + (r + r')^2$ and K is the complete elliptic integral of the first kind (Abramowitz & Stegun 1964). As $\rho \to 0$, K is logarithmically singular, so that G behaves like a two-dimensional source there. To reduce the number of unknowns, it is convenient in practice to remove the bottom $\partial\overline{B}_0$ from ∂S in (2.6) by augmenting $G(r, z; r', z')$ with its image source with respect to $z = -h$: $G(r, z; r', -z' - 2h)$.

For a particular $\partial S(t)$, (2.6) is a Fredholm integral equation of the first kind for ϕ_n on $\partial\overline{F}$ (where Dirichlet conditions are posed), and of the second kind for ϕ on ∂B. On the outer surface ∂S_0, however, neither ϕ nor $\partial\phi/\partial r$ are in principle known, and we shall obtain a closure by matching (patching) them to a general *linearized* solution $\tilde{\phi}$ outside S_0 which satisfies

$$\nabla^2\tilde{\phi} = 0, \quad r > A, \quad -h < z < 0, \tag{2.8a}$$

$$\left(\frac{\partial^2}{\partial t^2} + g\frac{\partial}{\partial z}\right)\tilde{\phi} = 0, \quad r > A, \quad z = 0, \tag{2.8b}$$

$$\frac{\partial\tilde{\phi}}{\partial n} = 0, \quad r > A, \quad z = -h, \tag{2.8c}$$

$$\tilde{\phi} \to 0, \quad r \to \infty, \quad t < \infty, \tag{2.8d}$$

and initial conditions

$$\tilde{\phi}, \frac{\partial\tilde{\phi}}{\partial t} = 0, \quad r > A, \quad z = 0, \quad t = 0. \tag{2.8e}$$

Details of the solution for $\tilde{\phi}$ are given in the Appendix. The important result is that the transient history of the potential $\tilde{\phi}$ and the normal derivative $\tilde{\phi}_n$ of any linear wavefield outside a closed surface S_0 can be directly related when evaluated on S_0. Thus we can write in general

$$\tilde{\phi}|_{S_0} = \mathrm{H}\tilde{\phi}_n|_{S_0}, \tag{2.9}$$

where H is a known operator (depending only on S_0) which accounts for both the impulsive motion of the fluid and the memory effect of the free surface outside S_0. Typically, H involves integration over the surface S_0 as well as a convolution of the operand for the memory effects (see Appendix). For a circular cylindrical S_0 (radius A, depth h), for example, the form of (2.9) is given by (A 8). Equation (2.9) now provides the closure for ϕ on S_0 upon imposing the matching conditions

$$\phi = \tilde{\phi}, \quad \phi_n = \tilde{\phi}_n, \quad \text{on } S_0. \tag{2.10}$$

Implicit in (2.10) is the assumption that S_0 is sufficiently large that the nonlinear radiated waves can be matched to a linear field without appreciable errors or reflection. The validity of this matching scheme must finally be demonstrated by, say, comparing results obtained using different values of the matching radii A for S_0. Substituting (2.9) into (2.6) using (2.10) we finally obtain

$$\alpha(r,z,t)\,\phi(r,z,t) = \int_{\partial B \cup \partial \overline{F}} r'\left(\frac{\partial \phi}{\partial n'} - \phi\frac{\partial}{\partial n'}\right) G\,\mathrm{d}\boldsymbol{x}' + \int_{\partial S_0} r'\left(G - \frac{\partial G}{\partial r'}\mathrm{H}\right)\frac{\partial \phi}{\partial r'}\,\mathrm{d}\boldsymbol{x}', \quad (r,z)\in\partial S. \tag{2.11}$$

Following a semi-Lagrangian approach, we have at a given time, the position of the body $\partial B(t)$ and the normal derivative ϕ_n on it given from the body boundary condition (2.3); the position $\partial\overline{F}(t)$ and ϕ on $\partial\overline{F}$ from time integration of (2.2); and a history of all previous values of ϕ_r on ∂S_0. Equation (2.11) can then be solved for ϕ on ∂B, ϕ_n (and hence $\nabla\phi$) on $\partial\overline{F}$ and (the present value of) ϕ_r on ∂S_0. The process is then repeated for successive time-steps. We remark here that the linear wavefield $\tilde{\phi}$ is completely general subject to (2.8) and appears in the formulation only through the function H in (2.11).

3. Numerical implementation

3.1. *Solution of the field equation*

To discretize (2.11), we (*a*) subdivide ∂S into a number of small segments ∂S_j, $j = 1, 2, \ldots, J$; (*b*) represent the boundary values of ϕ and ϕ_n by local basis functions; and (*c*) collocate (2.11) at selected points on ∂S. Since (2.11) represents mixed Fredholm integral equations of the first and second kind, the final linear algebraic system is solved using direct Gaussian elimination. An important consideration here is the treatment of the intersection point between $\partial\overline{F}$ and ∂B (and also between $\partial\overline{F}$ and ∂S_0) because of the anticipated weak singularity there. To avoid numerical difficulties at the intersection points, we follow the idea of Lin (1984) for the two-dimensional problem and seek to satisfy both the free-surface and body boundary conditions at the intersection. The most direct extension of the idea is to prescribe *both* ϕ from the condition on $\partial\overline{F}$ and ϕ_n from the body boundary condition at that point, i.e. at $\partial\overline{F} \cap \partial B$, we specify both ϕ_n on ∂B and ϕ, and solve for ϕ_n on $\partial\overline{F}$. This requires that the end points of the segments be specified as collocation points and that the approximation for ϕ be continuous across these points. We adopt the simplest choice of piecewise linear variations of (ϕ,ϕ_n) along each segment, prescribed

by their values, $(\phi_j, \phi_{nj}), j = 1, 2, \ldots, J+1$, at the segment end points. For consistency in approximation, and also to satisfy the need for continuous normal derivatives ϕ_n on $\partial\overline{F}$ where Dirichlet conditions are specified, we require that ∂S be at least piecewise quadratic with continuous slopes across segment boundaries. To avoid the degeneracy of quadratic splines, the portions of $\partial S(\partial B, \partial\overline{F}, \partial S_0)$ are approximated by cubic splines with prescribed slopes at the ends of each curve.

Thus within a particular segment j, ϕ^j and ϕ_n^j are linear functions of arc-length s,

$$[\phi_j(\xi), \phi_{nj}(\xi)] = (1-\xi)[\phi_j, \phi_{nj}] + \xi[\phi_{j+1}, \phi_{nj+1}], \tag{3.1}$$

where $\xi = s/L$, and s, L are respectively the arclength and total length of the segment given by

$$s(\zeta) = \int_0^\zeta J(\zeta')\,\mathrm{d}\zeta', \quad 0 \leqslant \zeta \leqslant 1, \tag{3.2a}$$

$$L = \int_0^1 J(\zeta')\,\mathrm{d}\zeta', \tag{3.2b}$$

and J is the Jacobian

$$J(\zeta) = \left[\left(\frac{\mathrm{d}r}{\mathrm{d}\zeta}\right)^2 + \left(\frac{\mathrm{d}z}{\mathrm{d}\zeta}\right)^2\right]^{\frac{1}{2}}, \quad 0 \leqslant \zeta \leqslant 1, \tag{3.2c}$$

which are all functions of the cubic spline parameter ζ, $0 \leqslant \zeta \leqslant 1$, for that segment. The difference between using a linear function of arclength ξ, and ζ in the interpolation (3.1) is non-trivial, since they differ, in general, even to leading order in L. Expanding (3.2a), for example, we have

$$\xi = \frac{J(0)}{L}(\zeta + O(L)). \tag{3.3}$$

Computationally, (3.1) is found to have a greater accuracy and more rapid convergence with segment length than linear basis functions based on ζ.

Following standard procedures, (2.11) can now be discretized and evaluated at successive collocation points $\boldsymbol{x}_j$, $j = 1, 2, \ldots, J+1$, to obtain a system of algebraic equations for the values of the unknowns (ϕ_j or ϕ_{nj}), $j = 1, 2, \ldots, J+1$. The quadrature over each segment typically involves products of the ring source G or its derivative, the interpolation functions in (3.1) and the Jacobian (3.2c) so that the integration is with respect to the parameter ζ. When the collocation point is an end point of the segment being integrated, special care is required to account for the singularities of the kernel. For the logarithmic singularity of G, the singular portions of the kernel up to and including $\zeta \ln(\zeta)$ are subtracted out and integrated analytically. There is no Cauchy singularity in $\partial G/\partial n$ when the collocation point $\boldsymbol{x}$ is on the interior of the boundaries ∂B, $\partial\overline{F}$ or ∂S_0, where the slope is continuous. The kernel can be evaluated (except at $\boldsymbol{x}' = \boldsymbol{x}_j$) and the included angle is simply $\alpha = 2\pi$. At the intersections of ∂B and $\partial\overline{F}$, and $\partial\overline{F}$ and ∂S_0, where the slopes are in general discontinuous, the integrand still exists at either side of $\boldsymbol{x}_j$ although somewhat more care is required to evaluate the included angle. When the body (or free surface) intersects the centreline $r = 0$, the integral is evaluated readily in a spherical coordinate system, so that for an inverted cone of half vertex angle θ_0, for example, the angle α at the vertex is $\alpha = 2\pi(1+\cos\theta_0)$. The evaluation of all the regular integrals are performed using four-point Gaussian quadratures, whose accuracies are confirmed against those obtained from convergent Romberg integrations.

For a given matching radius A, fixed (Eulerian) collocation points on ∂S_0, and prescribed time-steps, the evaluation of the functions in H need not be repeated for

different interior problems. For the impulsive part, the first two terms of (A 5) are evaluated and inverted once at the beginning of each problem. The singularities involved there are similar to those for G and will not be elaborated. The memory effects of H are evaluated via the last term of (A 8). A simple trapezoidal rule is used to perform the convolution integration, and the value $\phi_\tau(\tau = t)$ at the upper limit does not appear from this term on account of (A 11). When $z, z' \neq 0$, the integrand in the Fourier integral in (A 11) diminishes exponentially and Filon's method is used for its evaluation. For $z = z' = 0$, however, the integrand decreases only algebraically, and the convergence using Filon's quadrature is accelerated by subtracting out analytically the leading contributions in terms of sine and cosine exponential integrals.

3.2. *Time integration and stability*

Once (2.11) is solved for (ϕ, ϕ_n) on ∂S, $\nabla\phi$ can be evaluated on $\partial\overline{F}$, and the kinematic and dynamic boundary conditions (2.2) integrated in time. Provided that the desired accuracy is achieved, the specific time-integration formula used appears not to be critical and a variety of different schemes have been employed by previous investigators, typically using higher-order explicit (e.g. Runge–Kutta) or multi-step (e.g. Adam–Bashford–Moulton) methods or a combination of the two. In our simulations, we adopt a modified fourth-order Runge–Kutta scheme wherein the unknowns associated with the potential (ϕ, ϕ_n), but not the position of the boundary ∂S, are updated in the intermediate steps. This is not unlike the approach used by Dold & Peregrine (1986) where, for a given free-surface boundary, the (complex) potentials and its time derivatives are solved via Cauchy's integral theorem which are then combined in a higher-order time-integration formula. In the present case, computation time is dominated by that required to calculate the coefficients of the matrices associated with (2.11) so that the modified scheme, which maintains the same matrix coefficients during one complete time-step, represents a substantial saving in effort but at a slightly decreased accuracy compared to exact Runge–Kutta integration. Furthermore, the extra complication of tracing Lagrangian points which cross the computation boundary during the intermediate steps is avoided. To obtain the gradient $\nabla\phi = (\phi_r, \phi_z)$ or (ϕ_n, ϕ_s), the tangential derivatives ϕ_s are calculated by second-order finite-difference formulas in terms of arclengths. At the matching boundary, the position and potential value of the free-surface point on ∂S_0 for the new time-step are obtained by Lagrangian extrapolation.

Unless special care is taken, short-wavelength numerical instabilities, similar to those experienced by Longuet-Higgins & Cokelet (1976) and others for the two-dimensional problem, are also observed in our computations. The exact cause of these instabilities is uncertain although we believe that an important mechanism is the instability associated with concentration of Lagrangian points in regions of high flow gradients. If we perform a von Neumann stability analysis for the fourth-order Runge–Kutta scheme, for example, with linearized forms of the free-surface conditions (2.2), we obtain for stability the Courant condition

$$\Delta t^2 \leqslant \frac{8}{\pi}\frac{\Delta x}{g}, \tag{3.4}$$

where Δt is the time-step, and Δx the local grid spacing. This suggests that, for fixed Δt, such instabilities cannot be avoided for the nonlinear problem if the minimum grid size cannot be effectively controlled (i.e. (3.4) should at least be a necessary condition). Thus, we propose a scheme where a new set of equal-arclength spaced Lagrangian points on $\partial\overline{F}$ are created after every time-step. Using this algorithm, the

earlier instabilities are completely removed and no smoothing is required. Such a regriding idea is not new and has been used in related work by Fink & Soh (1974), for example, to improve the accuracy of their principal-value integrals and extend the simulation time of their calculation of two-dimensional unsteady vortex sheets. The main disadvantage of regriding is the potential loss of resolution which is usually provided by more closely spaced Lagrangian points in areas of large gradients (and conversely, because equal-arclength segments are used, unnecessarily fine resolutions may also be introduced in regions of small gradients). The advantages of regriding over smoothing especially in the present context are, however, substantial: (i) regriding can potentially alter the energy of the system much less, especially in the limit of very small grid sizes; (ii) the arbitrariness in the choice of a smoothing formula for a particular problem is avoided; (iii) smoothing cannot be easily applied at the intersection points between the free surface and body or matching boundaries; and (iv) the difficulties associated with the loss or gain of Lagrangian points as they cross the matching boundary are completely avoided if the free surface is regrided after every time-step.

3.3. *Numerical accuracy*

The overall accuracy of our numerical scheme can be considered in three parts: that associated with the solution of the field equation (2.11); that associated with the integration of the evolution equations (2.2); and that due to patching to the linear outer solution. Both the field-equation solver and the time-stepping procedure can be checked independently against known (prescribed) solutions. Our numerical experiments show that when forty segments are used per wavelength, the maximum relative error of the potential or its normal derivative on the boundary in (2.11) is less than 1 % in the interior and less than 4 % near the intersections of the free surface with the body or the matching boundary. The convergence with grid size is quadratic everywhere except at the intersection points where it is linear. Similarly, the modified fourth-order Runge–Kutta scheme has less than 1 % maximum relative error in the surface normal velocity or elevation after ten wave periods when forty time-steps are used per period. Discretizations comparable with these are used in all our computations. To assess the errors introduced by the matching boundary, our simulations are typically performed with two or more matching radii A, and convergence for results near the body is achieved to within several percent (e.g. see figure 8).

In addition to the above checks for convergence with respect to temporal and spatial discretizations and matching radii, the global accuracy of our computations is also evaluated for conserved fluid volume and conserved energy:

$$\iint_B p\frac{\partial\phi}{\partial n}\,\mathrm{d}\boldsymbol{x} = -\frac{\mathrm{d}}{\mathrm{d}t}\Big[\iint_{B\cup F\cup S_0}\tfrac{1}{2}\rho\phi\frac{\partial\phi}{\partial n}\,\mathrm{d}\boldsymbol{x}+\iint_{B\cup F}\tfrac{1}{2}\rho g z^2 n_z\,\mathrm{d}\boldsymbol{x}\Big]+\iint_{S_0}\rho\frac{\partial\phi}{\partial t}\frac{\partial\phi}{\partial n}\,\mathrm{d}\boldsymbol{x}. \tag{3.5}$$

The first term is proportional to the power expended by the body B, the second term to the rate of change of kinetic and potential energy in the fluid volume $\overline{V}$, and the last term to the energy flux across the matching boundary S_0. The pressure p on the body can be evaluated using Bernoulli's equation

$$-\frac{p}{\rho} = \frac{\partial\phi}{\partial t}+\tfrac{1}{2}|\nabla\phi|^2+gz = \left(\frac{\partial}{\partial t}+\boldsymbol{V}\cdot\nabla\right)\phi+(\tfrac{1}{2}\nabla\phi-\boldsymbol{V})\cdot\nabla\phi+gz, \tag{3.6}$$

where the second form is more useful when following moving points (with velocity $\boldsymbol{V}$) fixed on the body. For all the examples in §4, such quantities are typically conserved to within a few percent (e.g. see figure 9).

4. Numerical results

To demonstrate the usefulness and accuracy of our numerical method for axisymmetric problems involving free surfaces, we present results here for three different applications of interest. (i) Growth and collapse of an initially spherical cavity bubble near a free surface. For the non-buoyant case, excellent experimental data are available from Blake & Gibson (1981) which allow us to make a detailed comparison and validation of our code. It is found that the inclusion of gravity can have a profound effect on the evolution of the cavity. (ii) Large-amplitude periodic heaving motions of a floating vertical circular cylinder starting from rest. Our primary interests here are steady-state results for the reaction forces and flow field in the vicinity of the cylinder. Since a large number of periods must be simulated, especially for the latter, this is a particularly useful test of the effectiveness of the matching boundary. (iii) Forces and run-up on a heaving inverted cone. In addition to engineering applications such as the use of these devices as wavemakers, this problem also provides a demonstration that our treatment at the body and free-surface intersection line is satisfactory.

4.1. *Dynamics of a cavity bubble near a free surface*

We study the growth and collapse of a vapour cavity near an initially plane free surface under the assumptions of potential flow, negligible surface tension, vertical axisymmetry, and uniform and constant (in time) cavity-vapour pressure. The last assumption is made for simplicity and is not critical to our simulation. Physically, these assumptions are valid for cavities that are not too small (to ignore viscosity and surface tension), and for small liquid and vapour Mach numbers (to neglect compressibility effects and to assume constant cavity pressure), i.e. the fluid mechanics and thermodynamics of the vapour in the cavity are ignored. On the other hand, the assumption of axisymmetry may be unrealistic if the maximum volume of the bubble is greater than a few c.c., beyond which there may be considerable circumferential variations in the bubble shape and motion. The relevant parameters for this problem are $\eta = R_m/h$ and $\gamma = (gR_m)^{\frac{1}{2}}/U$, where R_m is the maximum radius the bubble will attain if the fluid is unbounded, h the initial depth of the centroid of the bubble, $U^2 = \Delta p/\rho$, and $\Delta p = p_a - p_v$, the (constant) difference between the atmospheric and cavity-vapour pressures. All velocities and lengths are scaled by U and R_m respectively. To begin the simulation, a spherical bubble of small initial radius $R_0 \ll h$ is used, whose velocity of expansion $\dot{R}_0$ is given by (Rayleigh 1917)

$$\dot{R}_0^2 = \tfrac{2}{3}U^2\left(\frac{R_m^3}{R_0^3} - 1\right). \tag{4.1}$$

In our simulations, $R_0/R_m = 0.25$ is used, which corresponds to a time $t_0 = 0.0154R_m/U$ measured from an instant when the bubble has negligible volume. Because of the short timescales involved, matching radiation boundaries are not necessary for these calculations and the simulations are conducted with rigid boundaries at $r = A = 4R_m$ and $z = -h = -5R_m$. Furthermore, to follow the large accelerations which are typical during the collapse phases, the time-step sizes are dynamically controlled so that the displacement of any particle on the surface does not exceed a fraction (typically 10 %) of the segment length.

For the non-buoyant case, $\gamma = 0$, detailed observations were made by Blake & Gibson (1981) who took 11000 frames/s cine pictures of the bubble under free-fall conditions. Figure 1 shows comparisons between the experiments (reproduced

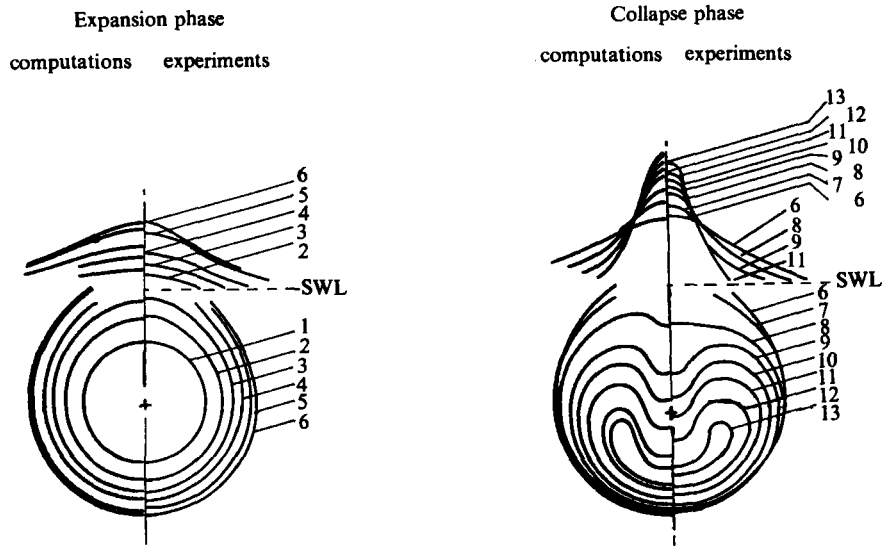

FIGURE 1. Comparison of profiles between measurements (Blake & Gibson 1981) and computations for the growth and collapse of a cavity bubble beneath a free surface ($\gamma = 0$ (no gravity) and $\eta = 1.02$) for different time instants. ——, initial free-surface position; +, initial centroid of the bubble.

directly from Blake & Gibson, figure 8) and our computations for the bubble profiles in the expansion and collapse phases for $\eta = 1.02$, and dimensionless times $t_k U/R_m = 0.087, 0.173, 0.260, 0.347, 0.520, 0.604, 0.867, 1.040, 1.214, 1.300, 1.387, 1.474, 1.508$; for the labels $k = 1, 2, \ldots, 13$. The collapse phase is marked by a rapid involution of the bubble in the form of a downward jet accompanied by a continually rising free surface which develops into a jet in the opposite direction. The correspondence between the experiments and calculations is satisfactory up to the last reported frame when the imploding jet is close to the bottom of the bubble. Our simulation, in fact, continues on to the time when the jet meets the far side of the bubble. These comparisons are substantially better both in terms of accuracy and duration of simulation than those of Blake & Gibson (1981) and Blake, Taib & Doherty (1985) using similar methods. (For example, computations for the same case in the former stopped after $t = t_9 = 1.214R_m/U$, and in the latter at $t = t_{10} = 1.3R_m/U$ with considerable distortions of the profile.) To obtain some understanding of the underlying dynamics, the centreline fluid velocity and total pressure are presented in figures 2 and 3 respectively for time instants corresponding to $k = 6, 9, 11, 12, 13$. (In this and later results, the velocity in the fluid is obtained directly in terms of ϕ and ϕ_n on the boundary from taking the gradient of Green's identity.) Note the large negative (downward) velocities of the jet above and a small distance away from the bubble. The magnitude, which increases with time, is close to $4U$ at $k = 13$, $tU/R_m = 1.508$. For $\Delta p \sim 1$ atmosphere and $\rho =$ density of water, this is approximately 40 m/s, a value which is somewhat smaller than, but of the same magnitude as, observed maximum velocities of bubble jets collapsing near a solid boundary (Plesset & Chapman 1971). The velocity below the bubble is relatively small but positive, indicating a rising of the bottom as the cavity collapses. Throughout the collapse phase, the total fluid pressure (figure 3) has a maximum value above the bubble which explains the directions of the free-surface and bubble-implosion jets.

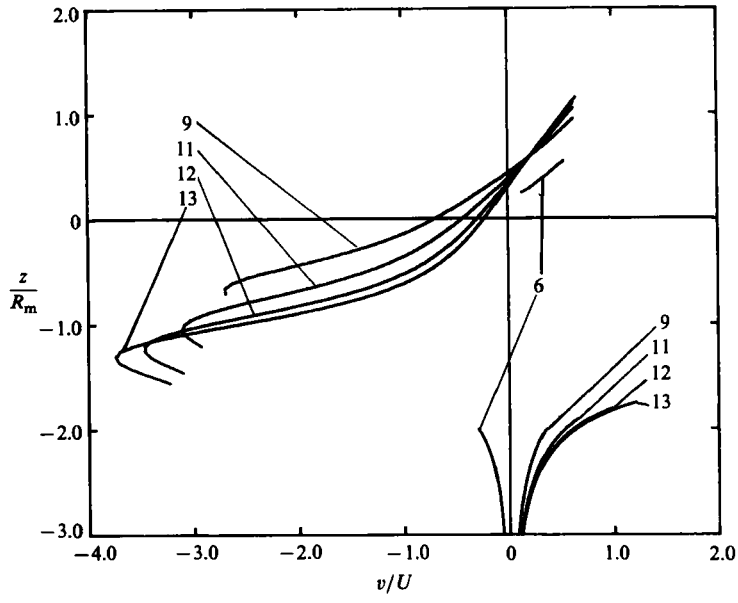

FIGURE 2. Centreline (vertical) fluid velocity near a cavity bubble collapsing beneath a free surface ($\gamma = 0$ (no gravity) and $\eta = 1.02$) for different time instants. Note that the curves are discontinued inside the bubble and above the free surface.

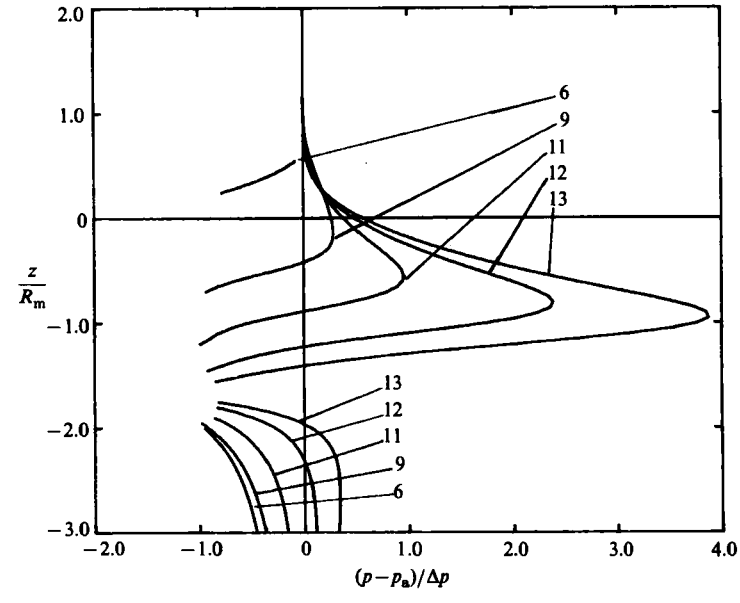

FIGURE 3. Centreline fluid pressure near a cavity bubble collapsing beneath a free surface ($\gamma = 0$ (no gravity) and $\eta = 1.02$) for different time instants. The pressure coefficient inside the bubble (-1) and above the free surface (0) are not plotted.

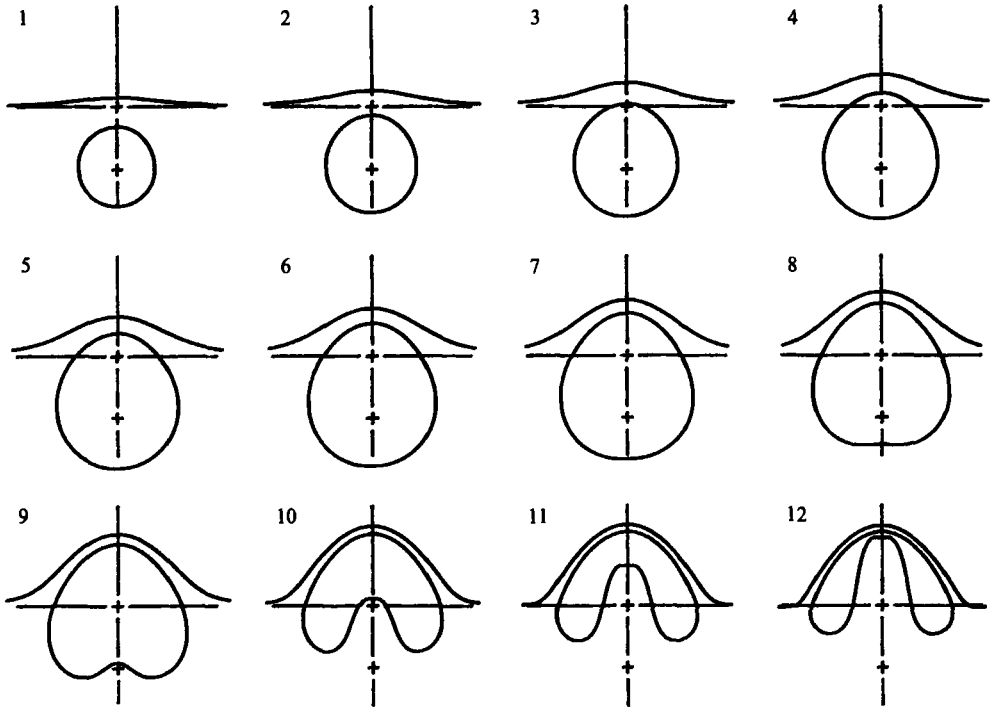

FIGURE 4. Profiles showing the growth and collapse of a vapour bubble beneath a free surface ($\gamma = 1$ (gravity present) and $\eta = 1$) for different time instants. Note that the crosses mark the initial free surface and bubble centroid locations.

At the last time instant plotted, the pressure reaches a maximum value of $(p-p_a)/\Delta p \sim 4$, which can be quite significant for small p_v.

When gravity is present, the evolution of the bubble can be changed dramatically (Blake *et al.* 1985). This is shown in figures 4–6 for the case $\eta = \gamma = 1$ (the definition is now $\Delta p = p_a + \rho g h - p_v$, and in fact $p_a = p_v$ in this case). Figure 4 shows the profiles of the cavity at dimensionless times $t_k U/R_m = 0.134$, 0.215, 0.311, 0.412, 0.521, 0.641, 0.777, 0.939, 1.148, 1.516, 1.716, 1.896; for the plots $k = 1, 2, \ldots, 12$. Because of the presence of buoyancy, the bubble (centroid) continues to rise through the growth and collapse phases eventually becoming entrained under an elevated free surface. The bubble collapse is now accompanied by the involution of its bottom surface into a jet which is directed upwards towards the free surface. At the last stages of our simulation, in fact, all three free surfaces are almost in contact with each other. In the centreline velocity plots, figure 5, the maximum velocities are associated with the upward jet but have magnitudes only about half of those in the non-buoyant case. The total centreline pressures (figure 6), which are dominated by hydrostatics at large depth, vary smoothly to the prescribed value p_v at the bubble, and also between the bubble and the free surface ($p_a = p_v$), in contrast to the profiles in figure 3. Furthermore, the maximum pressure is clearly no longer above the cavity, so that the implosion jet is directed from the bottom of the bubble upwards.

Provided that axisymmetry is maintained, it is seen that the present method is well suited to the study of the dynamics of cavity bubbles and their interactions with a free surface. The latter, in particular, may have useful applications, for example, to the generation of sub-sea acoustic signals using bubbles, and to the understanding of spray formation by entrained air.

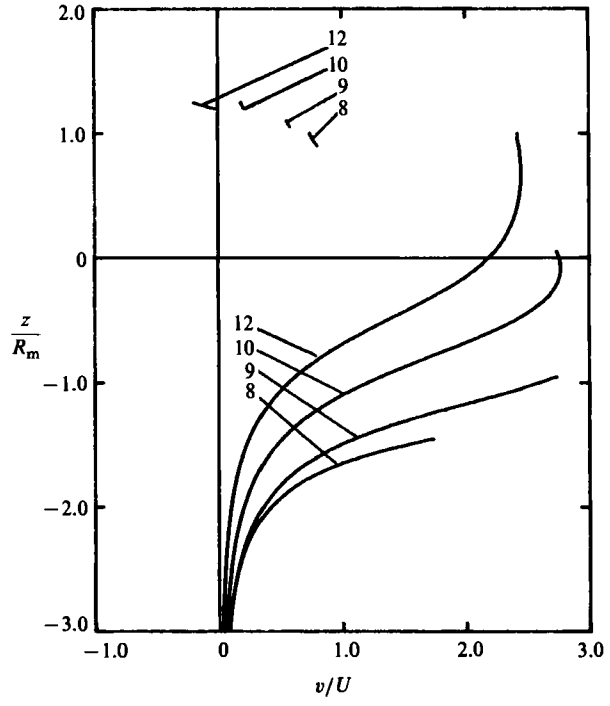

FIGURE 5. Centreline (vertical) fluid velocity near a cavity bubble beneath a free surface ($\gamma = 1$ (gravity present) and $\eta = 1$) for different time instants. Note that the curves are discontinued inside the bubble and above the free surface.

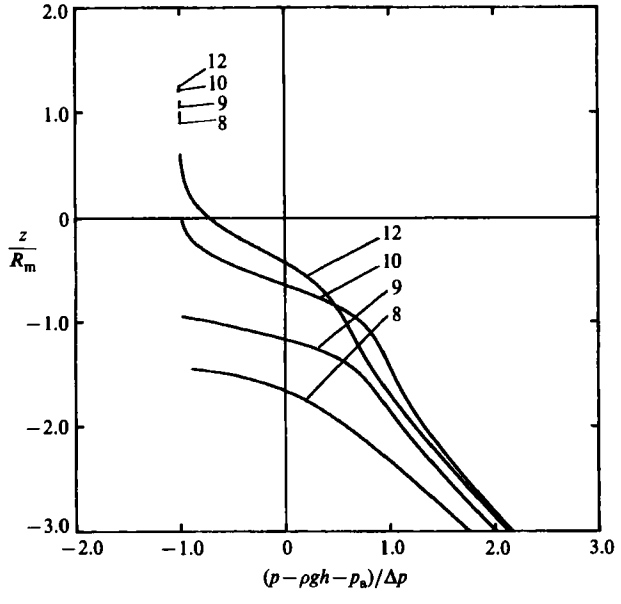

FIGURE 6. Centreline fluid pressure near a cavity bubble beneath a free surface ($\gamma = 1$ (gravity present) and $\eta = 1$) for different time instants. The pressure coefficients inside the bubble and above the free surface (both equal to -1) are not plotted.

4.2. *Forced heaving of a floating circular cylinder starting from rest*

We consider large-amplitude forced periodic heaving motions of a floating vertical circular cylinder of radius R_0, initial draught H, in water depth h, where $H/R_0 = 0.5$ and $h/R_0 = 1$. The vertical velocity of the cylinder is prescribed by

$$U(t) = \begin{cases} 0, & t < 0, \\ -\omega a \cos \omega t, & t \geqslant 0, \end{cases} \tag{4.2}$$

where the excitation frequency $\omega = 2\pi/T$ is chosen to correspond to an Airy wavelength of $2R_0$, i.e.

$$\frac{\omega^2 h}{g} = \pi \tanh \pi. \tag{4.3}$$

Three different (half) stroke amplitudes $a/H = 0.125, 0.25$ and 0.5 are considered. In the simulation for the largest amplitude $a/H = 0.5$ case, the cylinder is found to be already very close to aerating at the top of the stroke. When a matching radius of $A = 10R_0$ (i.e. 5 Airy wavelengths) is used, simulations have been carried out to beyond 12 wave periods. Uniform grid spacings are used on the free surface and matching boundary, while a cosine distribution of segment lengths is used on the cylinder in anticipation of the singular flow at the corner (see Newman 1985). In this case, we use a total of $N = 237$ unknowns (36, 180 and 20 segments on $\partial B, \partial\overline{F}$ and ∂S_0 respectively), and the solution time, which is roughly proportional to N^2, is of the order of 15 s per time-step on the Cray 2, or approximately 10 min per motion period.

Figure 7 shows time histories of the vertical force $f(t)$ on the cylinder calculated by three different methods for $a/H = 0.5$. Note that steady state for the force is reached within one or two periods. A relatively good estimate of the force can be obtained by considering only the impulsive force f_I associated with the *instantaneous* submerged portion of the body, $\boldsymbol{B}(t)$, below the still-water level. From momentum balance, we have

$$f_I(t) = -\rho \frac{\mathrm{d}}{\mathrm{d}t} \iint_{\boldsymbol{B}(t)} \psi n_z \,\mathrm{d}S + \tfrac{1}{2}\rho \iint_{B_0} \psi_r^2 \,\mathrm{d}S, \tag{4.4}$$

where $\psi(t)$ is the potential corresponding to the linear impulse (infinite-frequency) problem for $\boldsymbol{B}(t)$ satisfying $\psi = 0$ on $z = 0$, $r > R_0$, and $\psi_n = U(t) n_z$ on $\boldsymbol{B}(t)$. This is also computed and plotted in figure 7 for the $a/H = 0.5$ case. The rather close agreement indicates that the reaction force is dominated by added-mass effects as may be suggested by the rapid approach to steady state. In contrast, the linear time-domain result (obtained by keeping the free surface at $z = 0$ and ignoring nonlinear terms in our nonlinear code) shows fairly large discrepancies especially at the troughs. The difference between f_I and the nonlinear force represents radiated wave effects which show distinct higher-harmonic contributions. To see this, we perform harmonic analysis on the steady-state portion of the force, and define Fourier force coefficients

$$\left.\begin{aligned} &\frac{1}{T_0}\int_t^{t+T} f(t')\,\mathrm{d}t' = (\rho g \pi R_0^2 H)\left(\frac{a}{H}\right)^2 f_0^*, \\ \text{and} \quad &\frac{2}{T_0}\int_t^{t+T} f(t')\,\mathrm{e}^{\mathrm{i}n\omega t'}\,\mathrm{d}t' = (\rho g \pi R_0^2 H)\left(\frac{a}{H}\right)^n f_n^* \quad (n = 1, 2, \ldots,). \end{aligned}\right\} \tag{4.5}$$

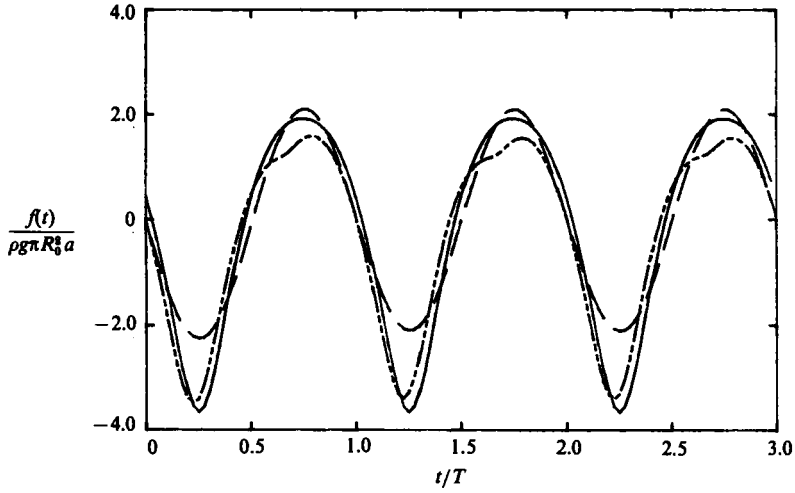

FIGURE 7. Time history of the vertical force on a floating cylinder for $a/H = 0.5$. ———, nonlinear force history; – – – –, impulsive force history $f_1(t)$ (equation 4.4); and ———, linear force history.

	f_0^*	$\lvert f_1^*\rvert$	$\lvert f_2^*\rvert$	$\lvert f_3^*\rvert$
Nonlinear computations				
$a/H = 0.5$	−0.45	2.19	1.3	0.6
$a/H = 0.25$	−0.42	2.14	1.2	0.6
$a/H = 0.125$	−0.40	2.11	1.2	0.7
Linear frequency–domain results	−0.31	2.118	—	—

TABLE 1. Harmonic force coefficients for the forced heaving of a floating cylinder

These are presented in table 1 where the hydrostatic force has been subtracted from f_1^*. Note that for the $a/H = 0.5$ case, the magnitudes of the mean, second and third harmonic forces are up to 11 %, 28 % and 7 % respectively of the first harmonic force. For comparison, we also calculate the mean and first-order force coefficients from a linear frequency-domain semi-analytic method which uses matched eigenfunction expansions outside and underneath the cylinder (e.g. Garrett 1971). Because of the scaling with respect to stroke amplitude in (4.5), the coefficients show only small deviations with decreasing strokes and approach the linear value for the first-harmonic force. The comparison with the frequency-domain mean force is not as close and is partly due to the difficulty in integrating the pressure near the corner. For $s = (R_0 - r)/R_0 \ll 1$, $\phi_r \sim s^{-\frac{1}{3}}$, and $p \sim \phi_r^2 \sim s^{-\frac{2}{3}}$; so that even for the linear calculation, the eigenfunction amplitudes theoretically have only a $-\frac{2}{3}$ power convergence.

For the flow field around the cylinder, the convergence to steady state is much slower than the forces acting on the cylinder. Figure 8 plots the instantaneous free-surface positions $\eta(r,t)$ at specific instants $t/T = 4, 6, 8$ and 10 for the case $a/H = 0.5$. Note that the matching boundary is located at $A/R_0 = 10$. The absence of reflections from that boundary is evidenced by the fact that the correspondence among the profiles, which indicates their approach to steady state, improves with increasing radius and time. (The slight irregularity near $r/R_0 = 1$ is numerical and is due to the cylinder nearly aerating at the top of its stroke.) To give an illustration

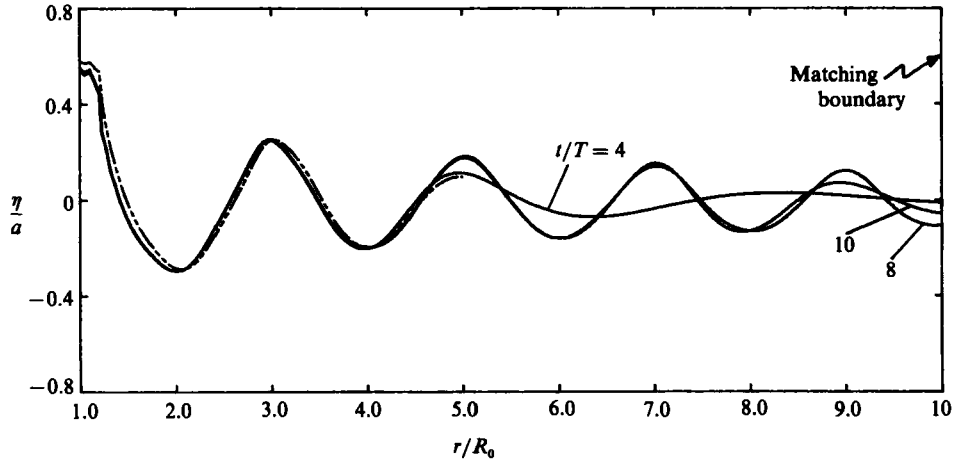

FIGURE 8. Instantaneous free-surface profiles outside a heaving vertical cylinder for $a/H = 0.5$ at different time instants $t/T = 4$, 8, 10, for a matching radius $A/R_0 = 10$ (———). Surface profile at $t/T = 4$ for a matching radius $A/R_0 = 5$ (– – – –).

of the convergence with matching radius A, the free-surface profile at $t/T = 4$ obtained using a much smaller computational domain $A/R_0 = 5$ is also shown. The use of the larger matching radius is clearly conservative. Figure 9 shows the conservation of energy for 12 periods of simulation for $a/H = 0.5$. We plot the left-hand side of (3.5), which represents the power input by the body, as well as ten times the difference between that and the rate of energy increase in the computational domain plus energy flux out of the matching boundary. This difference is less than 2% of the power for most of the range. The small jump near $t = (n+1/4)T$, $n = 0, 1, 2, \ldots$, occurs at the bottom of the stroke where the clearance is only $\frac{1}{4}R_0$. The added mass there is strongly affected by the bottom and the jump reflects the steep gradient of the added mass with small clearance.

The steady-state mean set-down associated with the nonlinear radiated waves is of some interest, and harmonic analyses of the steady-state surface profile histories are performed to obtain the coefficients $\eta_n^*(r)$, $R_0 < r < A$, defined by

$$\left.\begin{aligned} &\frac{1}{T_0}\int_t^{t+T} \eta(r,t')\,\mathrm{d}t' = \eta_0^*(r)\,H\left(\frac{a}{H}\right)^2\frac{R_0}{r} \\ \text{and}\quad &\frac{2}{T_0}\int_t^{t+T} \eta(r,t')\,\mathrm{e}^{-\mathrm{i}n\omega t'}\,\mathrm{d}t' = \eta_n^*(r)\,H\left(\frac{a}{H}\right)^n\left(\frac{R_0}{r}\right)^{n/2} \quad (n = 1, 2, \ldots). \end{aligned}\right\} \tag{4.6}$$

The forms of (4.6) are suggested by the asymptotic behaviour of the surface elevation $\tilde{\eta}_n^*$, based on first-order (frequency-domain) results assuming steady state. Thus, for a radiated wave of wavenumber k (satisfying $\omega^2 = gk\tanh(kh)$), we have (e.g. Mei 1983)

$$\left.\begin{aligned} &|\tilde{\eta}_1^*| \sim c \quad (kr \gg 1) \\ \text{and the mean set-down,}\quad &|\tilde{\eta}_0^*| \sim \frac{|c|^2 kH}{2\sinh 2kh} \quad (kr \gg 1). \end{aligned}\right\} \tag{4.7}$$

The amplitude coefficient c is a complex constant from linear frequency-domain analysis. Using the value of c from our semi-analytic linear calculations, the harmonic amplitudes η_n^* obtained from nonlinear simulations can be compared to the linear

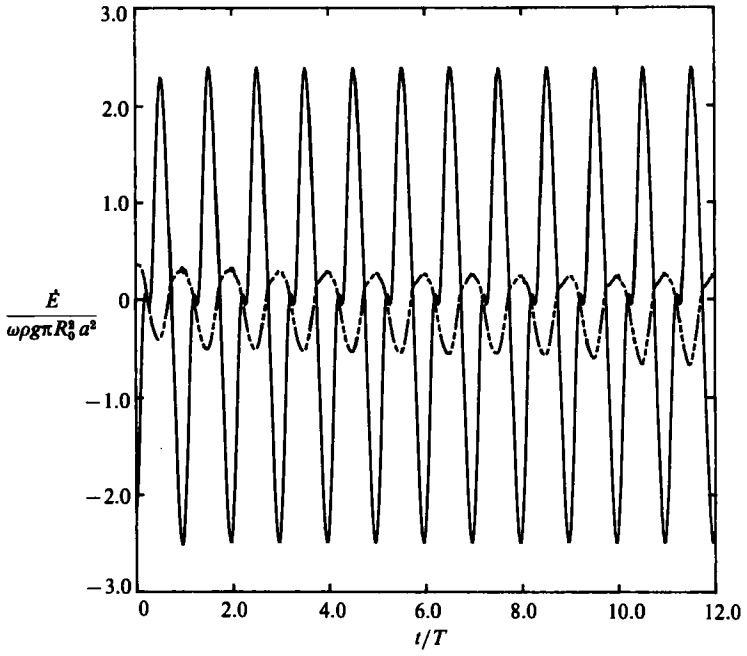

FIGURE 9. Numerical check of conservation of energy for a heaving circular cylinder, $a/H = 0.5$, equation (3.5). ———, the power $\dot{E}$ expended by the body; – – – –, ten times the difference between $\dot{E}$ and the rate of energy increase in the fluid plus energy flux out of S_0 (left- and right-hand sides of (3.5). Note that the energy is conserved to within 2% relative error for most of the 12 periods of motion.

asymptotics (4.7). This is shown in figure 10 for the first-harmonic and mean set-down. The comparison for η_1^* is quite satisfactory, reaching constant asymptotes whose values approach the linear estimate as stroke amplitude is decreased. The growing oscillations with radial distance give indications that steady state is not fully reached at the larger distances, while the oscillations themselves may be related to those behind an advancing wave front (e.g. Longuet-Higgins 1974). The result for η_0^* (figure 10*b*) is not as reasonable, with the nonlinear mean set-down remaining almost constant with increasing r. Although the magnitudes involved are quite small, this does indicate that the matching boundary does not adequately account for the mean second-order volume fluxes crossing it – a conclusion not completely surprising in view of the assumptions implicit in the matching conditions (2.11).

Finally, we show results for the fluid velocities near the body. Figure 11 is a vector plot of the steady-state time-averaged horizontal velocities in the fluid for $a/H = 0.5$. Near the surface, there is a mean outgoing Stokes' drift velocity compensated by a weaker return current which has an almost constant amplitude through the remaining water depth. A careful analysis of the magnitudes reveal that the mean velocities decrease with radial distance roughly as $1/r$ and quadratically with decreasing stroke amplitudes as expected.

4.3. *Forced heaving motion of a floating inverted cone starting from rest*

To test the validity of our treatment of the body and free-surface intersection line when the wall of the heaving body is not vertical, we consider the periodic forced motions of an inverted cone, initial waterplane radius R_0, draught $H = 2R_0$, and water

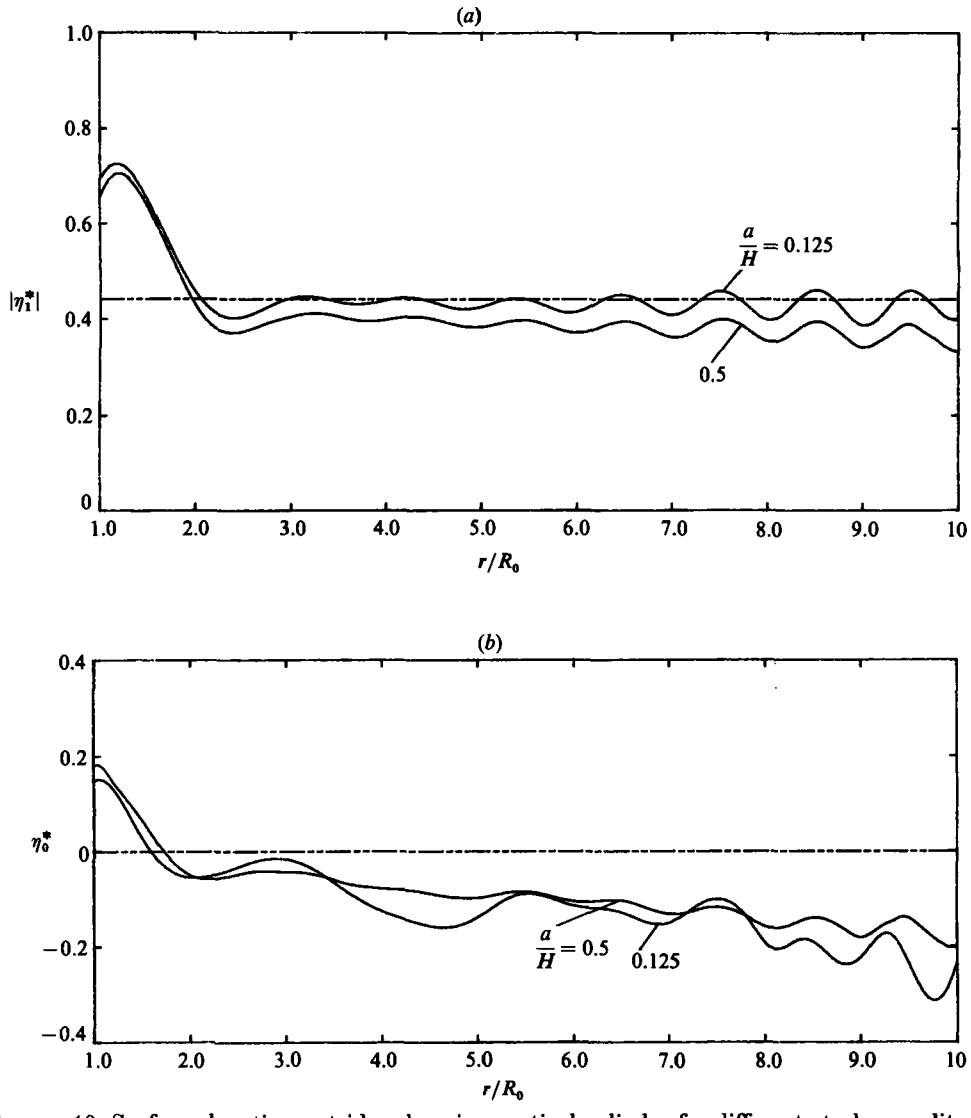

FIGURE 10. Surface elevation outside a heaving vertical cylinder for different stroke amplitudes. ———, nonlinear results; – – – –, constant asymptotes predicted by linear theory (equation 4.7) for (*a*) first-harmonic coefficient amplitude; (*b*) mean set-down coefficient.

depth $h = 2H$. We keep the same forcing velocity and frequency (4.2) and (4.3), and half-stroke amplitudes $a/H = 0.05$, 0.1 and 0.2 are considered. When larger amplitudes are used for this cone angle and frequency, a thin jet of fluid is observed to rise sharply up the side of the body, and the simulations cannot be continued much further. The matching boundary is placed at $A = 20R_0 = 5h$ and uniform segment lengths are used throughout.

Our primary interests here are the forces and run-up on the cone which reaches steady state rapidly and computations beyond four periods are found not to be necessary for our analyses. The reaction-force coefficients as defined earlier are given in table 2. (Note that the hydrostatic component is now included in the coefficients.) The linear frequency-domain results for comparison are now obtained using an

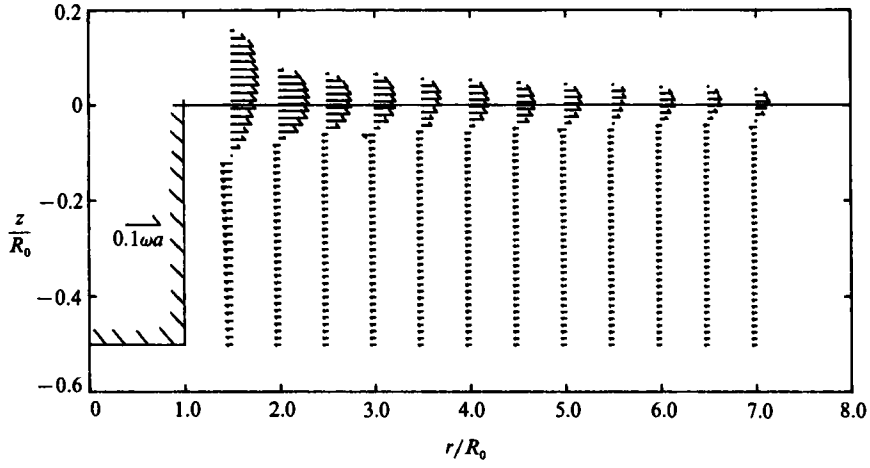

FIGURE 11. Mean horizontal velocities outside a heaving vertical cylinder for $a/H = 0.5$. The velocities continue almost constant to the bottom at $z/R_0 = -1$.

	f_0^*	$\lvert f_1^*\rvert$	$\lvert f_2^*\rvert$	$\lvert f_3^*\rvert$
Nonlinear computations				
$a/H = 0.2$	0.43	0.8270	0.24	0.072
$a/H = 0.1$	0.44	0.8242	0.25	0.073
$a/H = 0.05$	0.44	0.8238	0.25	—
Linear frequency–domain results	0.441	0.8237	—	—

TABLE 2. Harmonic force coefficients for the forced heaving of an inverted cone

axisymmetric hybrid element method (Yue, Chen & Mei 1978). As the motion amplitudes decrease, the coefficients compare well with linear predictions for both the mean and first-harmonic force, and there are no difficulties with large potential gradients. (For the third-harmonic coefficient, the force for the smallest stroke is insignificant and therefore not reliable.)

The behaviour at the contact point is very smooth, and figure 12 plots its position, (r_c, z_c), as a function of time after steady state is reached for $T \leqslant t \leqslant 4T$ for $a/H = 0.2$. Note the rapid approach to steady state indicated by the closed contour. The skewed shape of the particle orbit is due to the presence of nonlinearity. In general, if the vertical displacement of the cone is $\zeta(t)$ and the elevation of the free surface on the body is $\eta(r_c, t)$, then we have simply $z_c = \eta$ and $r_c - R_0 = (R_0/H)(\eta - \zeta)$. Now for the linear harmonic problem, if the forcing motion $\zeta(t)$ is sinusoidal, $\eta(r_c, t) \approx \eta(R_0, t)$ will also be sinusoidal with a particular magnitude and phase with respect to ζ. In this case, then, (r_c, z_c) describes the locus of an ellipse inclined at an angle to the vertical plane. Such a curve using the magnitude and phase values from our linear-theory calculation is also shown in figure 12. The difference between the linear and nonlinear predictions is quite significant.

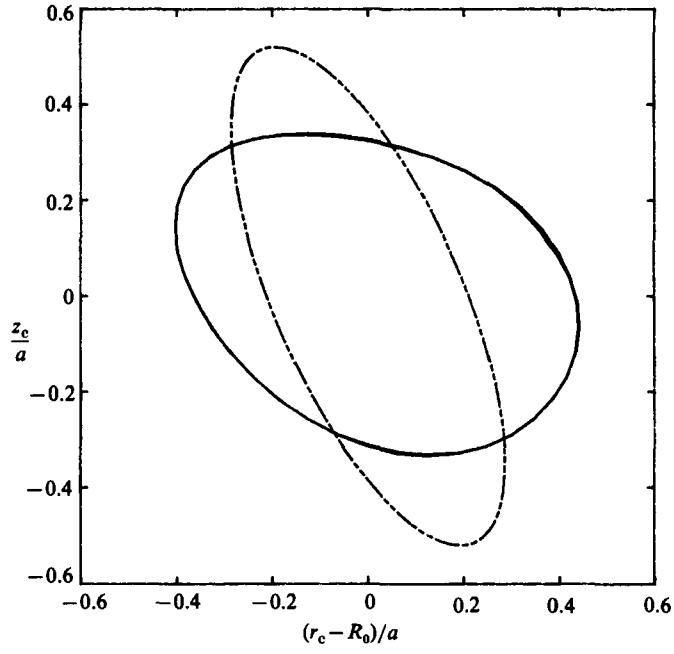

FIGURE 12. Steady-state locus of the intersection point between the free-surface and the surface of a heaving cone for $a/H = 0.2$. ———, nonlinear results; – – – –, particle orbit predicted from linear theory. Note that three periods of motion ($T \leqslant t \leqslant 4T$) are plotted from the nonlinear simulation.

5. Conclusion

A numerical method which extends the mixed Eulerian–Lagrangian approach to nonlinear axisymmetric body (or bubble) and wave interaction problems has been presented. For illustration, three problems involving nonlinear free-surface effects have been studied in some detail to bring out the important physical features and to demonstrate the effectiveness and accuracy of the method. In particular, novel ideas in the implementation of a linear far-field matching boundary, in the treatment of the free-surface and body intersection line, and in a regriding algorithm to suppress the instabilities have been tested and validated.

Our eventual objective is to develop accurate (quantitative) computational models for fully three-dimensional nonlinear body–free-surface interactions such as those associated with offshore structures in steep waves, large-amplitude ship motions, bow and stern flows, and nonlinear ship waves and wave resistance. To accomplish this, a number of important issues must be addressed:

(i) Treatment of the nonlinear free surface. The semi-Lagrangian method has been shown to be remarkably successful, in both two-dimensional and axisymmetric flows, especially in predicting highly nonlinear phenomena such as wave breaking and jets. The idea is directly applicable to three-dimensional flow, although refinements in the field-equation solver to achieve the necessary stability, accuracy and efficiency may be important.

(ii) The body and free-surface intersection line. Difficulties associated with the intersection points have been practically resolved by the method of Lin *et al.* (1984) in two dimensions in the context of complex-potential formulation, and extended to

axisymmetric flows using Green's identity in the present work. Further generalization to fully three-dimensional problems can be anticipated without special difficulties.

(iii) Far-field closure of the computational domain. The successful implementation of a far-field matching boundary has made feasible the long-time simulation of body-generated waves. For three-dimensional problems, the more general formulation (see Appendix) is still applicable. Algorithms for the efficient evaluation of the (linear) transient wave-source potential will be valuable.

(iv) Efficient solution of the field equation. The present formulation of the mixed boundary-value problem as a Fredholm integral equation of the first kind has required direct solutions of the resulting algebraic system. To discretize the computational boundary of realistic fully three-dimensional problems, $N = O(10^4)$ unknowns can be anticipated – a prohibitive number for direct solution even on modern supercomputers. Our experiences towards formulating the mixed problem entirely as second-kind Fredholm integral equations (Burton & Miller 1971; Baker *et al.* 1982), for which iterative solution procedures are applicable, have not been completely successful. This is partly due to difficulties associated with proper treatment of the intersection of the free surface with the body and the matching boundary. The development of an efficient iterative solution to the field equations in an irregular domain, perhaps even by non-boundary-integral methods, is of critical importance.

(v) Stability of the time integration. The regriding idea is very satisfactory at removing short-wavelength instabilities and should be directly extendable to three-dimensional problems (say with a two-dimensional spline of the surface). The exact mechanism of the instabilities is, however, still not well understood. A more fundamental treatment of this problem would be very desirable.

(vi) Implementation of a nonlinear incident wave for the diffraction problem. The difficulty here is to achieve this in a way consistent with a linear matching in the far field. Several promising ideas can be pursued: (*a*) generate steep incident waves in the interior through directional and/or frequency focusing of linear waves imposed on the matching circumference; (*b*) prescribe as initial conditions large-amplitude localized disturbances inside the computational domain; (*c*) introduce a wavemaker (for example a pressure patch or heaving cone) in the interior of the domain. However, since a good wavemaker will necessarily also be an efficient scatterer, simulation time will again be limited by the proximity of the wavemaker and thus the size of the computational region – a situation, ironically, not unlike what one may encounter in a physical wave tank.

Although a complete solution to these problems is still some time away, this work addresses many of the important issues and takes a useful step towards the simulation of realistic nonlinear free-surface and body interactions.

This research was supported by the National Science Foundation (NSF Grant MEA 8210649) and the Office of Naval Research (Contract N00014-82-K-0198). Most of the computations were performed at the NSF sponsored Minnesota Supercomputer Institute. D.K.P.Y. also acknowledges partial support from the Henry L. Doherty Chair.

Appendix. Solution of the linear outer problem

The requisite relationships (2.9) for the linear outer potential can be obtained by applying Green's theorem in the region $r > A$, $-h < z < 0$ and using the boundary conditions (2.8) to give

$$2\pi\tilde{\phi}(\boldsymbol{x},t)+\int_{S_0}\left(\tilde{\phi}(t)\frac{\partial}{\partial r'}-\frac{\partial\tilde{\phi}(t)}{\partial r'}\right)G_{\mathrm{R}}\,\mathrm{d}S' + \int_0^t \mathrm{d}\tau\int_{S_0}\left(\tilde{\phi}(\tau)\frac{\partial^2}{\partial\tau\,\partial r'}-\frac{\partial\tilde{\phi}(\tau)}{\partial r'}\frac{\partial}{\partial\tau}\right)G_{\mathrm{F}}(t-\tau)\,\mathrm{d}S' = 0, \quad \boldsymbol{x}\in S_0, \tag{A 1}$$

where G_{R}, G_{F} are respectively the impulsive (Rankine) and memory (free-surface) parts of the transient Green function source given by (Wehausen & Laitone 1960)

$$G_{\mathrm{R}}(x,y,z;x',y',z') = \frac{1}{R}+\frac{1}{R_1}-\frac{1}{R_2}-\int_0^\infty J_0(k[(x-x')^2+(y-y')^2]^{\frac{1}{2}}) \times\left(2\frac{\cosh k(z+h)\cosh k(z'+h)\,\mathrm{e}^{-kh}}{\cosh kh}-\mathrm{e}^{k(z+z')}\right)\mathrm{d}k, \tag{A 2}$$

$$G_{\mathrm{F}}(x,y,z;x',y',z';t) = 2\int_0^\infty \mathrm{d}k\frac{\cosh k(z+h)\cosh k(z'+h)}{\sinh kh\cosh kh} \times\{1-\cos([gk\tanh kh]^{\frac{1}{2}}t)\}J_0(k[(x-x')^2+(y-y')^2]^{\frac{1}{2}}). \tag{A 3}$$

In (A 2), $R_1^2 = (x-x')^2+(y-y')^2+(z+z'+2h)^2$ and $R_2^2 = (x-x')^2+(y-y')^2+(z+z')^2$ are associated respectively with Rankine source singularities at image points about the bottom and free surface.

When the flow is vertically axisymmetric, the integrals over θ' in (A 1) can be performed analytically. Using (2.7) and the identity (Watson 1952)

$$\int_0^{2\pi} J_0(k[(r'\cos\theta'-r)^2+r'^2\sin^2\theta']^{\frac{1}{2}})\,\mathrm{d}\theta' = 2\pi J_0(kr)J_0(kr') \tag{A 4}$$

we have

$$2\pi\tilde{\phi}(r=A,z,t)+\int_{-h}^0 \mathrm{d}z'\left(\tilde{\phi}(t)\frac{\partial}{\partial r'}-\frac{\partial\tilde{\phi}(t)}{\partial r'}\right)\bar{G}_{\mathrm{R}}|_{r=A} + \int_0^t \mathrm{d}\tau\int_{-h}^0 \mathrm{d}z'\left(\tilde{\phi}(\tau)\frac{\partial^2}{\partial r'\,\partial\tau}-\frac{\partial\tilde{\phi}(\tau)}{\partial r'}\frac{\partial}{\partial\tau}\right)\bar{G}_{\mathrm{F}}(t-\tau)|_{r=A} = 0, \tag{A 5}$$

with the 'ring' transient Green functions given by

$$\bar{G}_{\mathrm{R}}(r,z;r',z') = G(r,z;r',z')+G(r,z;r',-z'-2h)-G(r,z;r',-z') -2\pi r\int_0^\infty \mathrm{d}k\left(2\frac{\cosh k(z+h)\cosh k(z'+h)\,\mathrm{e}^{-kh}}{\cosh kh}-\mathrm{e}^{k(z+z')}\right)J_0(kr)J_0(kr'), \tag{A 6}$$

$$\bar{G}_{\mathrm{F}}(r,z;r',z',t-\tau) = 4\pi r\int_0^\infty \mathrm{d}k\frac{\cosh k(z+h)\cosh k(z'+h)}{\sinh kh\cosh kh} \times\{1-\cos[(gk\tanh kh)^{\frac{1}{2}}(t-\tau)]\}J_0(kr)J_0(kr'). \tag{A 7}$$

Computationally, the integral in (A 6) converges rapidly with k because the Rankine singularities are subtracted out. The quadrature in (A 7), however, requires special care because of the oscillatory nature of both the cosine and Bessel functions. Note that (A 5) is not explicitly in the form of (2.9) because of the appearance of $\tilde{\phi}(t)$ under

the first integral. ($\tilde{\phi}_r(t)$ does not come from the convolution integral since $\overline{G}_F(x, x'; 0) = 0$ as required). Numerically, one simply inverts the kernel associated with $\tilde{\phi}(t)$ after discretization to obtain H explicitly. Since ∂S_0 is fixed, that kernel is a function only of h and A (and the discretization of ∂S_o) and the inversion needs to be performed once only for a given simulation.

Alternatively, one can seek an equation of the form (2.9) directly. For any linearized axisymmetric wavefield, $\tilde{\phi}$ and $\tilde{\phi}_r$ on a fixed vertical cylinder of radius A can, in general, be related by an equation of the form (Lin *et al.* 1984):

$$\tilde{\phi}(A,z,t) = \int_{-h}^{0} \mathrm{d}z' D_R(z,z') \tilde{\phi}_r(A,z',t) + \int_0^t \mathrm{d}\tau \int_{-h}^{0} \mathrm{d}z' D_F(z,z',t-\tau) \tilde{\phi}_r(A,z',\tau) \quad (-h < z < 0), \quad \text{(A 8)}$$

where D_R represents the impulsive contributions, and D_F the free-surface memory effects of the 'Green function', $D(r,z,t;r',z',\tau)$ which satisfies the linearized exterior problem (2.8) with the condition

$$\frac{\partial D}{\partial r} = \delta(z-z')\,\delta(t-\tau), \quad r = A, \quad -h < z, z' < 0. \quad \text{(A 9)}$$

The result is similar to that of Lin *et al.* (1984) for infinite depth and is simplified when values on $r = A$ only are required. The final forms are

$$D_R(z,z') = -\frac{2A}{\pi^2} \int_0^\infty \mathrm{d}k \left(\mathrm{e}^{-k|z-z'|} + \mathrm{e}^{-k(z+z'+2h)} - \frac{2\cosh k(z+h)\cosh k(z'+h)\,\mathrm{e}^{-kh}}{\cosh kh} \right) \frac{1}{(kA)^2[J_1^2(kA)+Y_1^2(kA)]} \quad \text{(A 10)}$$

and

$$D_F(z,z',t-\tau) = -\frac{4g}{\pi^2} \int_0^\infty \mathrm{d}k \frac{\sin[(gk\tanh kh)^{\frac{1}{2}}(t-\tau)]}{(gk\tanh kh)^{\frac{1}{2}}} \times \frac{(1+\tanh kh)\cosh k(z+h)\cosh k(z'+h)\,\mathrm{e}^{-kh}}{(kA)(J_1^2(kA)+Y_1^2(kA))\cosh kh}. \quad \text{(A 11)}$$

As expected, D_R is logarithmically singular as $z \to z'$, while at $\tau = t$, we have $D_F(z,z',0) = 0$.

Comparing the earlier Green's theorem formulas (A 5), (A 6), (A 7) to the present results (A 8), (A 10), (A 11), we note that the former can be more readily generalized to three-dimensional problems although (A 11) for D_F is in a more efficient form for quadrature than (A 7) for $\overline{G}_F$. Both results are equally valid, and since portions of the Rankine kernel (A 6) are almost identical with that already required for the interior problem, we use (A 6) for the impulsive part, and (A 11) for the free-surface memory part of H in (2.9) for our computations.

REFERENCES

Abramowitz, M. & Stegun, I. A. 1964 *Handbook of Mathematical Functions*. Government Printing Office, Washington.

Baker, G. R., Meiron, D. I. & Orszag, S. A. 1982 Generalized vortex methods for free-surface flow problems. *J. Fluid Mech.* **123**, 477–501.

Blake, J. R. & Gibson, D. C. 1981 Growth and collapse of a vapour cavity near a free surface. *J. Fluid Mech.* **111**, 123–140.

Blake, J. R., Taib, B. B. & Doherty, G. 1985 Transient cavities near boundaries. Part II – Free Surface. University of Wollongong Preprint No. 5/86.

BURTON, A. J. & MILLER, G. F. 1971 The application of integral equation methods to the numerical solution of some exterior boundary-value problems. *Proc. R. Soc. Lond.* A323, 201–210.

DOLD, J. W. & PEREGRINE, D. H. 1986 An efficient boundary-integral method for steep unsteady water waves. *Numerical Methods for Fluid Dynamics II* (ed. K. W. Morton & M. J. Baines), pp. 671–679. Oxford University Press.

FALTINSEN, O. M. 1977 Numerical solution of transient nonlinear free-surface motion outside or inside moving bodies. In *Proc. 2nd Intl Conf. on Num. Ship Hydro., U.C. Berkeley* (ed. J. V. Wehausen & N. Salvesen), pp. 347–357. University Extension Publications.

FINK, P. T. & SOH, W. K. 1974 Calculation of vortex sheets in unsteady flow and applications in ship hydrodynamics. In *Proc. 10th Symp. on Naval Hydro., Cambridge, Mass* (ed. R. D. Cooper & S. W. Doroff), pp. 463–491. Washington: Government Printing Office.

GARRETT, C. J. R. 1971 Wave forces on a circular dock. *J. Fluid Mech.* **46**, 129–139.

GREENHOW, M. & LIN, W. M. 1983 Nonlinear free surface effects: experiments and theory. *MIT, Dept. of Ocean Engineering, Rep. No.* 83-19.

GREENHOW, M., VINJE, T., BREVIG, P. & TAYLOR, J. 1982 A theoretical and experimental study of the capsize of Salter's duck in extreme waves. *J. Fluid Mech.* **118**, 221–239.

ISAACSON, M. DE ST. Q. 1982 Nonlinear-wave effects on fixed and floating bodies. *J. Fluid Mech.* **120**, 267–281.

KRAVTCHENKO, J. 1954 Remarques sur le Calcul des Amplitudes de la Houle Lineaire Engendree par un Batteur. In *Proc. 5th Conf. on Coastal Engineering, Grenoble, France* (ed. J. W. Johnson), pp. 50–61. Council on Wave Research, France.

LIN, W. M. 1984 Nonlinear motion of the free surface near a moving body. Ph.D. thesis, MIT, Dept. of Ocean Engineering.

LIN, W. M., NEWMAN, J. N. & YUE, D. K. 1984 Nonlinear forced motions of floating bodies. In *Proc. 15th Symp. on Naval Hydro., Hamburg* (Chairman: O. Krappinger), pp. 33–49. Washington: National Academy Press.

LONGUET-HIGGINS, M. S. 1974 Breaking waves – in deep or shallow water. In *Proc. 10th Symp. Naval Hydro., Cambridge, Mass* (ed. R. D. Cooper & S. W. Doroff), pp. 597–605. Washington: Government Printing Office.

LONGUET-HIGGINS, M. S. & COKELET, E. D. 1976 The deformation of steep surface waves on water. I. A numerical method of computation. *Proc. R. Soc. Lond.* A350, 1–26.

MEI, C. C. 1983 *The Applied Dynamics of Ocean Surface Waves.* Wiley.

MILOH, T. 1980 Irregularities in solutions of the nonlinear wave diffraction problem by vertical cylinder. *Proc. ASCE J. Waterway, Port, Coastal and Ocean Div.* **106**, 279–284.

MOORE, D. W. 1981 On the point vortex method. *SIAM J. Sci. Stat. Comput.* **2**, 65–84.

NEWMAN, J. N. 1985 Transient axisymmetric motion of a floating cylinder. *J. Fluid Mech.* **157**, 17–33.

PLESSET, M. S. & CHAPMAN, R. B. 1971 Collapse of an initially spherical vapour cavity in the neighbourhood of a solid boundary. *J. Fluid Mech.* **47**, 283–290.

RAYLEIGH, LORD 1917 On the pressure developed during the collapse of a spherical cavity. *Phil. Mag.* **34**, 94–97.

ROBERTS, A. J. 1983 A stable and accurate numerical method to calculate the motion of a sharp interface between fluids. *J. Appl. Math.* **31**, 13–35.

VINJE, T. & BREVIG, P. 1981 Nonlinear ship motions. In *Proc. 3rd Intl Symp. Num. Ship Hydro., Paris* (Chairmen: J. C. Dern & H. J. Haussling), pp. 257–268. Bassin d'Essais des Carènes, France.

VINJE, T., MAOGANG, X. & BREVIG, P. 1982 A numerical approach to nonlinear ship motion. In *Proc. 14th Symp. on Naval Hydro.* (Chairman: I. F. Ogilvie), pp. 245–278. Washington: National Academy Press.

WATSON, G. N. 1952 *A Treatise on the Theory of Bessel Functions.* Cambridge University Press.

WEHAUSEN, J. V. & LAITONE, E. V. 1960 Surface waves. *Handbuch der Physik*, vol. 9, pp. 446–778. Springer.

YUE, D. K., CHEN, H. S. & MEI, C. C. 1978 A hybrid element method for diffraction of water waves by three-dimensional bodies. *Intl J. Numer. Meth. Engng* **12**, 245–266.